Petroleum Science 23 (2026) 4193–4203

Contents lists available at ScienceDirect

Petroleum Science

journal homepage: www.keaipublishing.com/en/journals/petroleum-science

Original Paper

Unveiling the multiscale dissolution pathways of asphaltene deposits in a natural deep eutectic solvent (NaDES)

Ya-Han Liu [a], Xin-Yi Ma [a], Ding-Kai Hu [a], Qiang Wang [a], Peng Wei [a,*], Hui Sun [a,b,**]

[a] Key Laboratory of Oil and Gas Fine Chemicals, Ministry of Education & Xinjiang Uygur Autonomous Region, College of Chemical Engineering, Xinjiang University, Urumqi, 830046, Xinjiang, China
[b] School of Chemical Engineering, East China University of Science and Technology, Shanghai, 200237, China

ARTICLE INFO

Article history:
Received 12 October 2025
Received in revised form
10 April 2026
Accepted 13 April 2026
Available online 17 April 2026

Edited by Yan-Hua Sun

Keywords:
Natural deep eutectic solvents
Asphaltene
Molecular interactions
Microfluidic dissolution

ABSTRACT

Heavy crude oil contains high levels of asphaltenes, which tend to aggregate and deposit in reservoir pores and pipelines, severely hindering recovery, transportation, and refining. To address the challenge of enhancing asphaltene stability and preventing operational blockage, a green, low-toxicity natural deep eutectic solvent (NaDES) composed of thymol and tetradecylamine (TDA) was developed in this study. This solvent exhibits a high asphaltene solubility of ~75 mg/mL at 25 °C. Density-functional theory (DFT) calculations revealed that the dissolution is governed by hydrogen bonding (notably between $-NH_2$ in NaDES and S=O in asphaltene) and dispersive interactions. Key mechanisms include interfacial adhesion and wetting (adhesion force of −6.7 nN, contact angle of ~0°), penetration and diffusion (diffusion area ratio of 4.5), layer-to-layer exfoliation into micro-nano sheets, and improved dispersion stability. Microfluidic experiments in rough asphaltene-filled channels further demonstrated flow-dependent dissolution pattern transition from wedge-shaped to uniform, accompanied by significant surface smoothing. This work presents an efficient and sustainable NaDES-based strategy to mitigate asphaltene deposition in heavy oil production and transportation, supporting higher resource recovery, lower operational costs, and improved process sustainability.

1. Introduction

In China's northwestern oilfields, heavy oil extraction faces the core challenge of asphaltene deposition. Asphaltene, often termed “petroleum cholesterol”, precipitates from crude oil under specific conditions, forming solid deposits that clog reservoirs and pipelines. This severely impairs production capacity and incurs substantial subsequent treatment costs. Asphaltene molecules are characterized by a polycondensed aromatic core surrounded by naphthenic and aromatic rings, along with alkyl side chains of varying lengths that often contain heteroatoms such as sulfur, nitrogen, and oxygen (Barrera et al., 2013). Their aggregation behavior follows the Yen–Mullins model. Through interactions such as π-π stacking (Mullins et al., 2012), they can form multilevel aggregates ranging from nanoscale clusters to larger fractal structures, ultimately leading to deposition (Fig. 1(a)).

Deep eutectic solvents (DES), introduced by Abbott et al. (2003), are a class of ionic liquid analogues that align with green chemistry principles. Formed by mixing hydrogen bond acceptors and donors in specific ratios, they exhibit depressed melting points due to hydrogen bonding. DES offer significant research potential due to their advantages, such as low cost, low vapor pressure, high thermal stability (up to 275 °C), recyclability, and simple preparation methods like heating or stirring. Consequently, they are widely used in material synthesis (Długosz and Banach, 2024; Parsai et al., 2024), extraction (Sukor et al., 2021), catalysis (Shafique et al., 2025), electrochemistry (Lan et al., 2021), and drug dissolution (Ainurofiq et al., 2018; Zainal-Abidin et al., 2019). Several DES have been investigated as potential asphaltene inhibitors. For instance, Hebbar et al. (2023) employed molecular dynamics (MD) simulations and optical microscopy to study the behavior of reline, glyceline, and ethaline in separating asphaltenes from toluene/*n*-heptane solutions. Jahangiri et al. (2017)

* Corresponding author.
** Corresponding author.
E-mail addresses: weipeng369@xju.edu.cn (P. Wei), sunhui@ecust.edu.cn (H. Sun).
Peer review under the responsibility of China University of Petroleum (Beijing).

https://doi.org/10.1016/j.petsci.2026.04.015

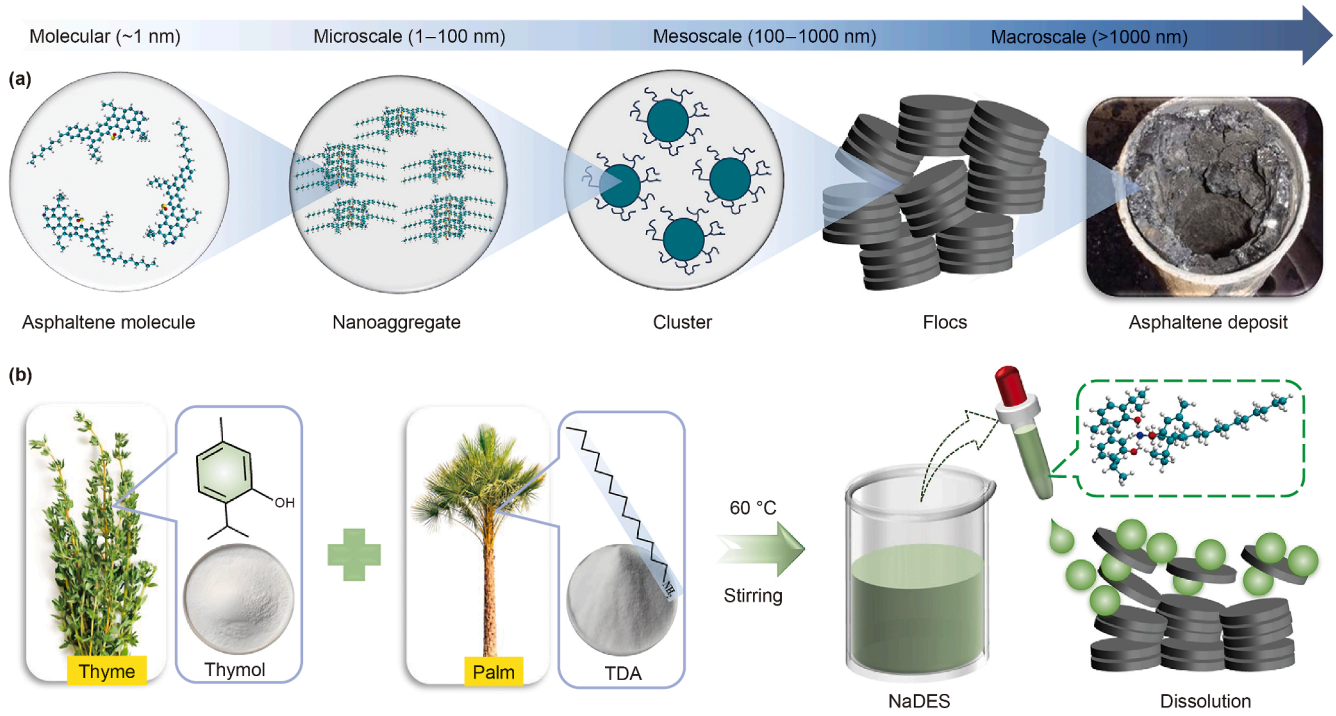

Fig. 1. (**a**) Schematic of asphaltene aggregation. (**b**) Schematic of NaDES composed of thymol and TDA for asphaltene dissolution.

synthesized a 1:1 DES from choline chloride and monoethylene glycol, using UV-vis spectroscopy to determine the asphaltene precipitation onset and evaluate the efficacy of DES in improving asphaltene stability. Conductor-like screening model for real solvents (COSMO-RS) has proven valuable for solvent screening due to its predictive capability and qualitative accuracy (Benguerba et al., 2019; Lemaoui et al., 2020a, 2020b). Neni et al. (2024) employed COSMO-RS computational screening to evaluate 153 potential HBA:HBD combinations (HBD: hydrogen bonding donor; HBA: hydrogen bonding), which efficiently identified muscimol-based DES as a highly promising candidate for asphaltene solubilization.

Despite these advances, there is still a key limitation in the current research that needs to be addressed: the kinetic mechanism of DES dissolving asphaltene in complex real environments is not yet clear (Slavov et al., 2024). The current assessment mainly relies on turbidity and transmittance measurements under static conditions, but such results are difficult to predict the actual effects in dynamic flow environments. Therefore, microfluidic devices are used to better study the dissolution kinetics; their scale can simulate near-well and reservoir pores and can achieve direct observation, and have been successfully applied to many studies of crude oil and asphaltene (Conn et al., 2014; Kim et al., 2013). However, few studies have addressed how dissolution alters surface roughness, resulting in irregular flow channels that govern pore-scale solute transport and influence localized dissolution rates (You and Lee, 2021). Therefore, direct pore-scale observations are critical to correlate the evolution of surface roughness with dissolution dynamics in rough channels containing asphaltene deposits.

This study designed a green low-melting-point solvent based on thymol and tetradecylamine (TDA) for efficient dissolution of asphaltene (Fig. 1(b)). Through COSMO-RS screening, the thymol/TDA system was selected from 676 potential formulations, and the microscopic mechanism of the dissolution process was clarified by quantum chemical calculations in density-functional theory (DFT). Through multi-scale experiments such as dissolution, precipitation, wettability, and adsorption, the dissolution performance of natural deep eutectic solvent (NaDES) was systematically evaluated. Finally, based on microfluidic technology, the visualization observation and quantitative analysis of the pore-scale dissolution kinetics of NaDES in asphaltene-saturated rough channels were achieved. This study provides a new idea for multi-scale asphaltene dissolution and supports the development of clean production technologies.

2. Experimental section

2.1. Materials

Thymol (purity ≥98%), tetradecylamine (TDA, purity ≥96%), dodecylbenzenesulfonic acid (DBSA, purity ≥96%) were both purchased from Shanghai Macklin Biochemical Co., Ltd. Asphaltene particles were extracted from the heavy oil from oil wells in the Northwest Petroleum Bureau, Urumqi, Xinjiang. Toluene (purity ≥99.9%) used for the separation of heavy oil components was purchased from Sigma-Aldrich, and *n*-heptane (purity ≥99%) was purchased from Tianjin Kemiou Chemical Reagent Co., Ltd. The deionized water used was made in the laboratory.

2.2. Methods

NaDES was synthesized from methyl salicylate and TDA by a one-pot method. The resulting NaDESs were characterized using Fourier-transform infrared spectroscopy (FT-IR) and proton nuclear magnetic resonance (^{1}H NMR). The thermal stability of NaDESs was measured using a thermogravimetric-differential scanning calorimeter (TG-DSC). On this basis, the dissolution behavior, interfacial interactions, and structural evolution of asphaltenes in NaDES were systematically investigated through a combination of experimental and computational methods. Experimental measurements included solubility determination,

particle size analysis, detection of the flocculation onset point by ultraviolet-visible spectroscopy, contact angle measurement, and characterization by atomic force microscopy, electron microscopy, Fourier transform infrared spectroscopy, and X-ray diffraction. Theoretical calculations covered molecular structure optimization, energy calculation, independent gradient model for hydrogen-bonded systems (IGMH) and solubility prediction using the COSMO-RS model. Additionally, the changes in the solid–liquid interface morphology during the dissolution process were characterized using microfluidic experiments by quantitatively analyzing surface roughness factors. Detailed experimental information can be found in Supplementary Information.

3. Results and discussion

3.1. Characterization of NaDES

In this study, NaDES was synthesized via a one-step method using thymol (HBD) and TDA (HBA). The prepared mixtures with thymol to TDA molar ratios of 2:3, 2:2, 3:2, 4:2, 6:2, and 8:2 exhibited distinct physical states at room temperature. Systems with molar ratios of 2:3 and 8:2 showed partial melting, appearing as solid–liquid mixtures or wet paste-like forms. In contrast, homogeneous liquid phases were formed at ratios of 2:2, 3:2, 4:2, and 6:2, confirming the successful formation of NaDES under these specific compositional conditions (Fig. 2(a)). This result indicates that the phase behavior of the thymol-based NaDES system is composition-dependent.

As shown in Fig. 2(b), the spectroscopic analysis reveals characteristic features of the thymol/TDA system. (1) The broad O–H stretching vibration of thymol (3500–3100 cm^{-1}) and N–H stretching vibrations of TDA (3500–3300 cm^{-1}) undergo significant changes upon NaDES formation (Chutia et al., 2018; Jiang et al., 2025). (2) In NaDES, the disappearance of a N–H stretching vibration at 3155 cm^{-1} and a weak and broad band at 3360 cm^{-1} are observed, which possibly corresponds to stretching from $–NH_2$ (Benítez et al., 2011). (3) The peak of thymol near 1000 cm^{-1} corresponds to a specific C–O in the aromatic ring (Ar), which becomes weak and broad in NaDES (Gao et al., 2024). These transformations demonstrate the enhanced hydrogen bonding interactions between thymol's phenolic hydroxyl and TDA's primary amine (O–H···N). However, the aliphatic C–H stretching vibrations (2800–3000 cm^{-1}) from both components are unaffected. These verify that the NaDES formation is primarily governed by strong hydrogen bonding interactions.

The ^1H NMR spectra presented in Fig. 2(c) demonstrate the formation of the NaDES through distinct spectral changes. In the spectrum of pure thymol, characteristic signals are observed at 4.75 ppm (phenolic –OH) and 3.15 ppm (isopropyl –CH– group). Upon NaDES formation, several significant spectral modifications occur: (1) the complete disappearance of thymol's hydroxyl proton signal at 4.75 ppm, (2) the appearance of a new upfield-shifted signal at 5.14 ppm, which gradually shifts further upfield to 4.27 ppm with decreasing thymol concentration, and (3) a slight upfield shift (3.23–3.27 ppm) of the isopropyl –CH– group signal. These spectral changes provide compelling evidence for the establishment of hydrogen bonding interactions between thymol's phenolic hydroxyl group (acting as hydrogen bond donor) and TDA's primary amine group (serving as hydrogen bond acceptor). The collective NMR observations unambiguously confirm the successful formation of a hydrogen-bonded DES system through these specific molecular interactions.

According to IGMH analysis, the non-covalent interactions between thymol and TDA were clearly visualized (Fig. 2(d)). Specifically, a blue isosurface was observed between the phenolic hydrogen atom of thymol and the nitrogen atom of TDA, corresponding to the highest peak in the scatter plot (sign $(\lambda_2)\rho \approx -0.048$ a.u., $\delta g \approx 0.08$ a.u.) (Fan et al., 2021). This indicates a strong electrostatic attraction, confirming the presence of an O–H···N hydrogen bond. Meanwhile, a greenish-blue isosurface was formed between the phenolic oxygen atom and the hydrogen atom of thymol, corresponding to a secondary peak in the scatter plot (sign$(\lambda_2)\rho \approx -0.03$ a.u., $\delta g \approx 0.05$ a.u.), suggesting an O–H···O hydrogen bond. These results demonstrate that strong electrostatic interactions, particularly the O–H···N hydrogen bond, play a crucial role in facilitating the binding between thymol and TDA to form NaDES.

The thermal stability of the synthesized NaDESs was evaluated through TGA/DTG analysis conducted at 30–300 °C (Fig. 2(e)). The thermograms revealed that the NaDESs underwent mass loss in two distinct stages. The first stage, occurring between 40 and 80 °C with minimal mass loss (<2.0%), likely resulted from the evaporation of adsorbed water molecules (Majka et al., 2025). The second and more substantial decomposition stage (>90% mass loss) commenced at approximately 140 °C, representing the true thermal degradation of the NaDESs. DTG analysis indicated peak decomposition rates within 180–200 °C, a temperature range near 50 °C lower than previously reported for natural oxymatrine/lauric acid-based NaDES systems (Fan et al., 2021). This difference is attributed to charge-assisted hydrogen bonding in the current system. Furthermore, the thermal stability of NaDESs with varying molar ratios was found to be significantly influenced by thymol content, as this component demonstrated relatively lower thermal resistance at elevated temperatures.

3.2. Quantum-chemical analysis of NaDES–asphaltene interactions

3.2.1. Thermodynamic affinity between NaDES and asphaltenes based on COSMO-RS

This study systematically screened 676 deep eutectic solvent (DES) formulations, which were constructed from 26 hydrogen bond donors (HBDs, primarily phenolic compounds and organic acids) and 26 hydrogen bond acceptors (HBAs, including organic amines and alcohols) at various molar ratios (Tables S4 and S5, and Figs. S2 and S3). The selected HBDs and HBAs cover a broad range of chemical functionalities commonly utilized in DES applications for hydrocarbon processing. Among these, the thymol/TDA combination demonstrated optimal asphaltene solubility and selectivity.

The COSMO-RS model quantitatively predicts the infinite dilution activity coefficients ($\ln\gamma^{\infty}$) and excess enthalpies (H^E) for DES–asphaltene systems, revealing their molecular affinity (Alioui et al., 2020). As shown in Fig. 3(a), $\ln\gamma^{\infty}$ becomes more negative (from −2.0 to −4.8) with increasing thymol content, indicating enhanced solubility at higher thymol concentrations. The corresponding negative H^E values confirm exothermic mixing, driven by strong intermolecular forces such as hydrogen bonding and π-π interactions. Complementary σ-profile and σ-potential analyses provide further molecular insight (Fig. 3(b)). The charge density distribution is divided into three regions: HBD ($\sigma < -0.0082$ e/Å^2), nonpolar ($-0.0082 < \sigma < 0.0082$ e/Å^2), and HBA ($\sigma > 0.0082$ e/Å^2) (Lemaoui et al., 2020a,b; Neni et al., 2024). Both asphaltenes and DES components exhibit predominantly nonpolar character (due to alkyl groups) along with moderate polar contributions, which correlates directly with their superior solubilization performance.

3.2.2. Electrostatic potential analysis of NaDES–asphaltene interactions

From Fig. 4(a), the electrostatic potential (ESP) mapping reveals that the negative potential regions of NaDES (minimum: −21.70 kcal/mol) are localized around hydroxyl oxygens and benzene rings, while

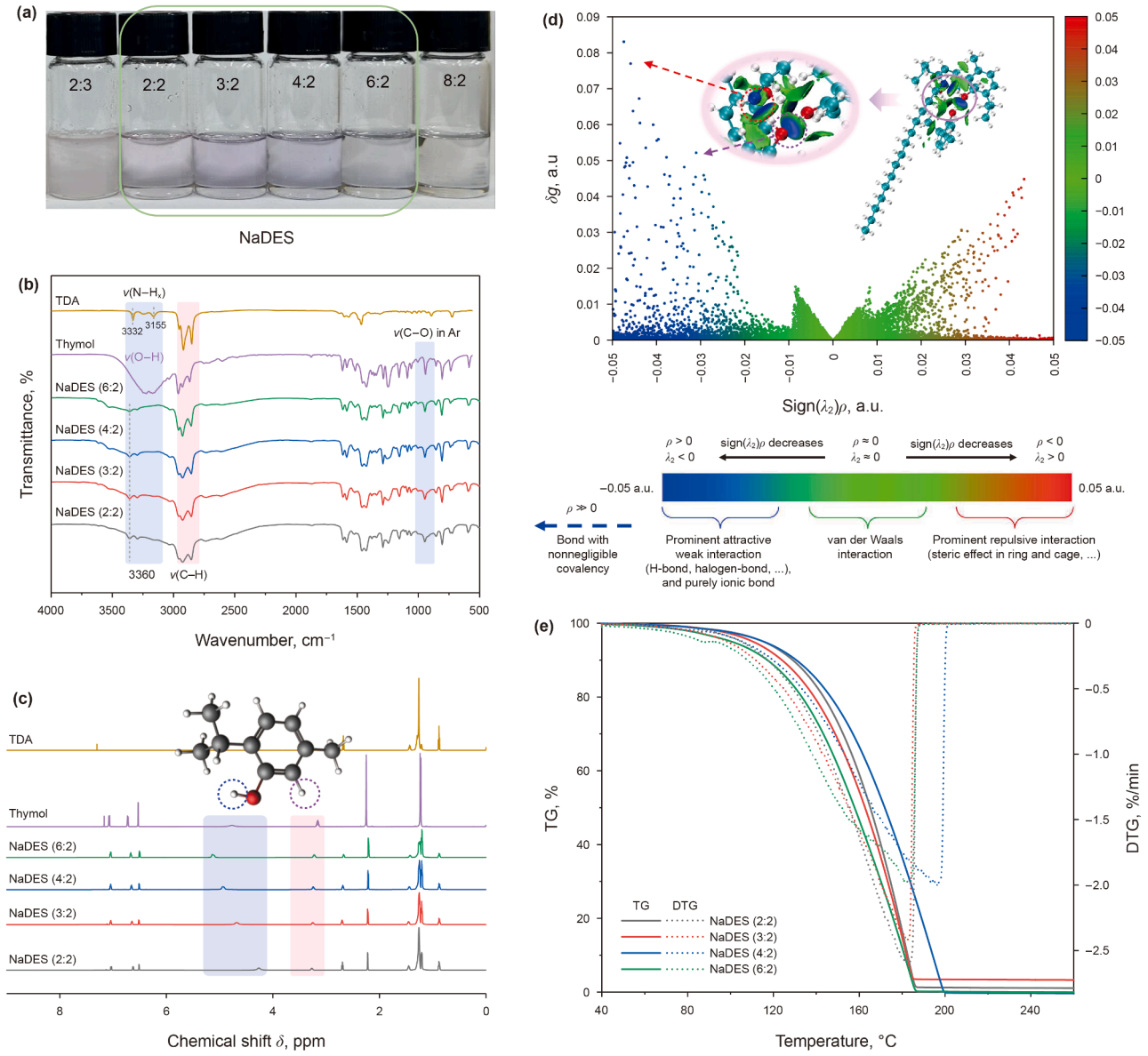

Fig. 2. (**a**) Synthesis process of NaDESs: thymol and TDA were stirred together at 60 °C. FT-IR (**b**) and ^{1}H NMR (**c**) spectra of NaDES and its components. (**d**) Analysis of thymol/TDA molecular ion pairs via the independent gradient model based on Hirshfeld partition (IGMH): scatter plots of δg versus sign(λ_2)ρ and their corresponding color-filled isosurfaces. (**e**) TG/DTG curves of NaDESs.

its positive potential regions (maximum: 36.97 kcal/mol) are concentrated on the amino group (Altamash et al., 2018). Conversely, asphaltene molecules exhibit a strong negative potential (minimum: −44.45 kcal/mol) near sulfoxide groups adjacent to benzene rings and a positive potential (maximum: 23.63 kcal/mol) around nitrogen atoms. This complementary charge distribution facilitates targeted molecular attraction. Specifically, the penetration diagram (Fig. 4(b)) demonstrates that the positive ESP maximum of NaDES (–NH_2) and the negative ESP minimum of asphaltene (S=O) overlap at an interatomic distance shorter than the sum of their van der Waals radii. This geometric signature confirms the formation of a strong, directional hydrogen bond (O=S···H–N), rather than a weak, nonspecific van der Waals contact (Kumar et al., 2024). Therefore, the effective dissolution of asphaltenes by NaDES results from a synergistic mechanism in which charge-directed hydrogen bonds and broad van der Waals interactions jointly promote molecular dispersion.

These computational results, obtained from optimized structures (Fig. 4(b)), demonstrate a strong non-covalent interaction in the NaDES–asphaltene cluster, evidenced by a negative interaction energy of −38.55 kcal/mol. This value aligns with that reported for a vanillic acid–diphenyl ether DES system (−27.26 kcal/mol) and substantially exceeds the typical range for pure asphaltene systems (from −7.17 to −11.95 kcal/mol) (Behloul et al., 2022; Sellaoui et al., 2017), collectively supporting a hydrogen-bond-dominated interaction mechanism.

3.2.3. IGMH/QTAIM analysis of noncovalent interactions

Analysis of the IGMH plot (Fig. 4(c)) indicates that hydrogen bonding and van der Waals forces act as the primary driving forces

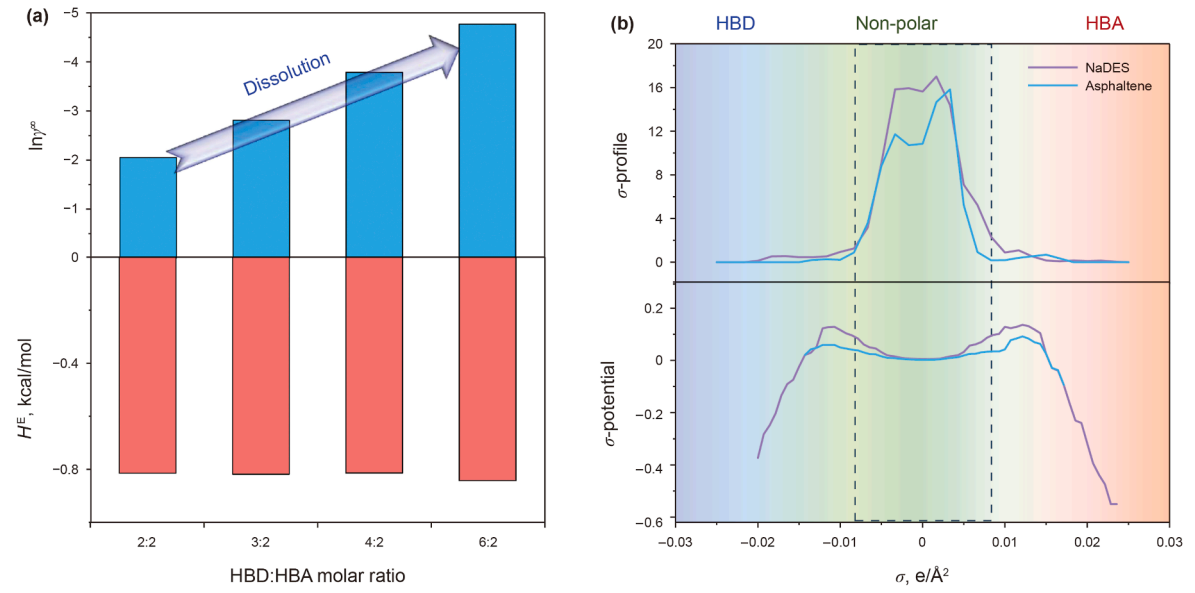

Fig. 3. (**a**) Infinite dilution activity coefficient (lnγ^{∞}) and excess enthalpy (H^E) of DESs with asphaltenes at varied HBA:HBD ratios. (**b**) σ-profile and σ-potential.

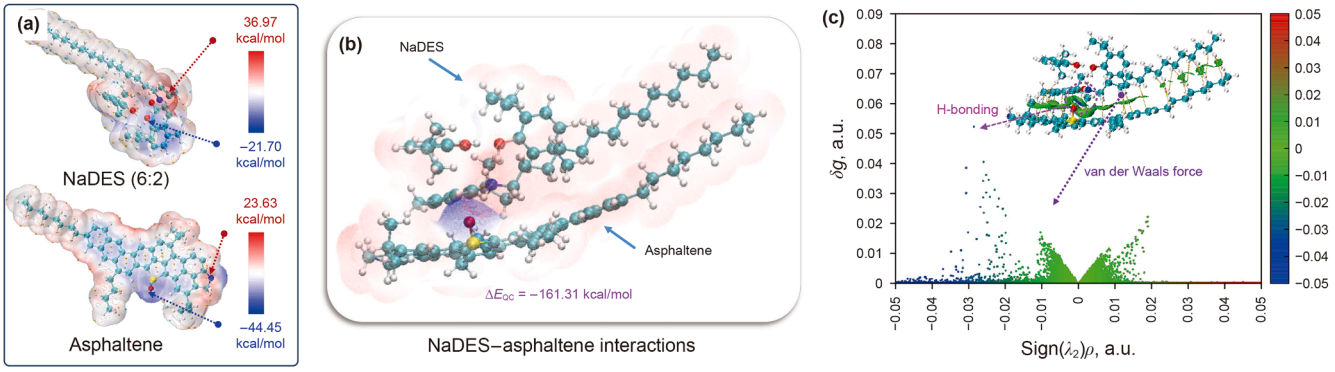

Fig. 4. (**a**) Electrostatic potential distribution on van der Waals surface. (**b**) Penetration diagram between DES and asphaltene, and the interaction energy ΔE_{QC} between NaDES and asphaltene. (**c**) Analysis of NaDES–asphaltene molecular ion pairs via IGMH: scatter plots of δg versus sign(λ_2)ρ and their corresponding color-filled isosurfaces.

in the NaDES–asphaltene system (Emamian et al., 2019). Isosurface visualization demonstrates that NaDES molecules form hydrogen bonds with oxygen atoms in sulfoxide groups of asphaltenes, exemplified by specific contacts such as N–H···O=S. The extensive green isosurface regions signify strong attractive dispersion interactions. These forces mainly arise from van der Waals contacts between NaDES and the aromatic rings of asphaltenes (likely involving π-π stacking) as well as between their alkyl chains, consistent with the spatial arrangement of these moieties.

QTAIM analysis (Table S7) shows positive electron density (ρ_{BCP}) and $\nabla^2\rho_{BCP}$ values at all BCPs in the NaDES–asphaltene complexes, verifying the existence of closed-shell noncovalent interactions (Emamian et al., 2019). The calculated binding energies (E(H)) at hydrogen-bonding sites indicate weak interactions, which reflects their mixed dispersive and electrostatic character. Notably, the N–H···O hydrogen bond between the sulfoxide oxygen (–S=O) in asphaltene and the amino group (–NH_2) in NaDES electron density and binding energy are $\rho_{BCP} = 0.0285$ a.u. and $E(H) = -5.63$ kcal/mol, classifying it as a weak-to-medium hydrogen bond (Wang et al., 2022). This results from the sulfoxide lone-pair electrons acting as hydrogen-bond acceptors, while the nitrogen-containing groups in NaDES serve as hydrogen-bond donors.

3.3. Solvation of asphaltenes in NaDES

Fig. 5(a) illustrate the dissolution performance of NaDES on asphaltene. As demonstrated, the dissolution efficiency of asphaltenes in NaDES increases with rising temperature. The NaDES with an HBD:HBA molar ratio of 3:2 has the highest solubility. At lower temperatures (25 °C), the solubility of asphaltenes reaches approximately 75 mg/mL, which is significantly higher than the 8−10 mg/mL reported in the literature for toluene/*n*-heptane mixed solvents (2:3 v/v) (Li et al., 2021). This enhanced performance is attributed to the presence of phenolic hydroxyl and amino groups in the NaDES, which form strong hydrogen-bonding interactions with asphaltenes. Furthermore, the structure of the NaDES allows the alkyl chains of fatty acids and the non-polar regions of phenols to interact more effectively with the asphaltene phase, thereby enhancing solubility (Trenzado et al., 2023).

The morphological evolution of asphaltene particles in NaDES was documented at different time intervals (0, 2, 4, 6, and 8 h) under magnetic stirring at 500 rpm, as shown in Fig. 5(b). After 2 h of stirring, the average particle size of asphaltenes decreased from 105 to 50 μm. This indicates that NaDES induces fragmentation or cracking of asphaltene aggregates through strong solvation effects. With prolonged reaction time, particle size progressively reduced

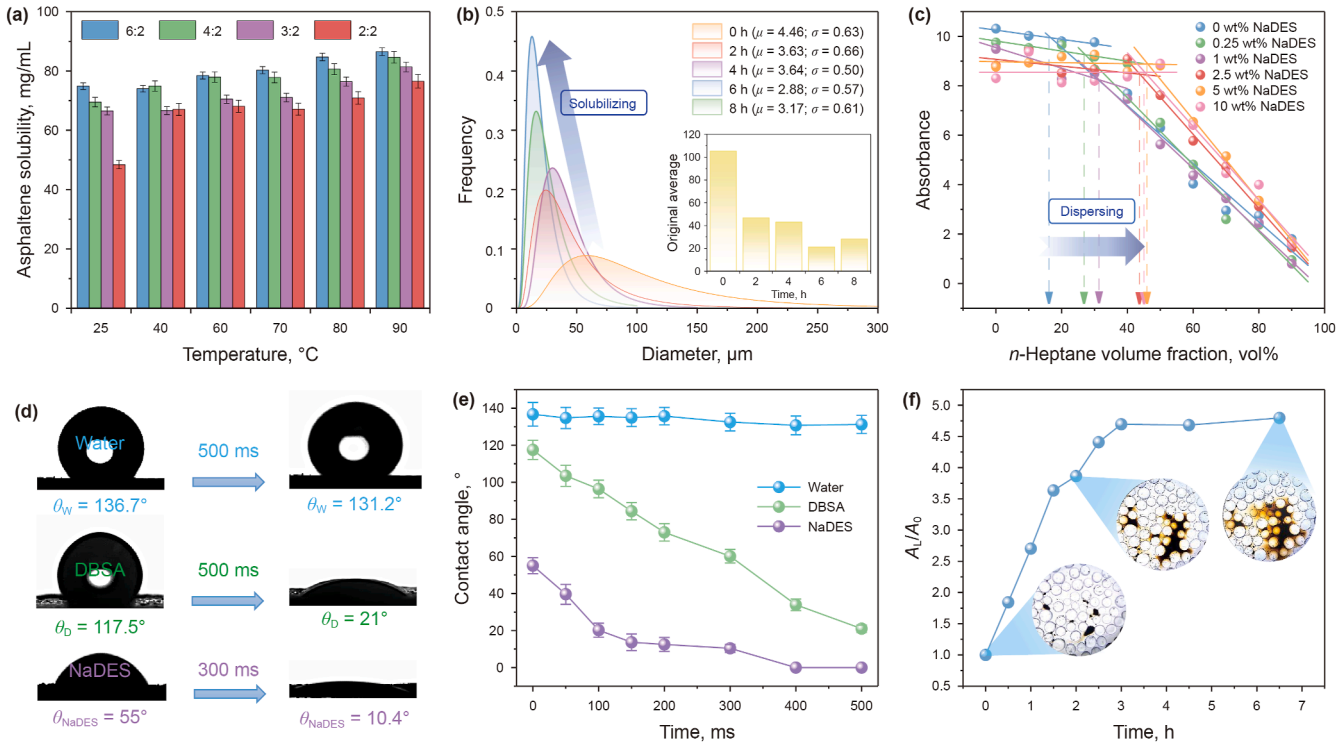

Fig. 5. (**a**) Impact of NaDES component ratios on dissolution performance. (**b**) Morphological evolution of asphaltene particles in NaDES (μ and σ denote variance and mean, respectively; the calculation formula is given in Eq. (S6) of Supplementary Information). (**c**) Effect of NaDES on the flocculation onset of asphaltenes in the *n*-heptane/toluene solvents. (**d**) Appearance of the contact angle between asphaltenes and the solvents, i.e., water, dodecylbenzenesulfonic acid (DBSA), and NaDES, and (**e**) the contact angle changes over time. (**f**) The static dissolution process of asphaltenes in the porous media, where the blue scale bar (the length of the scale in the first figure) is 2 mm (A_L is the diffusion area at a given time; and A_0 is the initial area).

to approximately 20 μm after 6–8 h of stirring. These macroscopic observations demonstrate the exceptional capability of NaDES to dissolve asphaltene aggregates. Fig. 5(c) presents flocculation onset measurements determined by UV-vis spectroscopy. Without the addition of NaDES, the onset of asphaltene flocculation was observed as low as at ~16 vol% (*n*-heptane volume fraction). However, the addition of NaDES shifts this onset significantly to ~45 vol%, representing a more than twofold increase in stability. NaDES molecules form extensive hydrogen bonds with asphaltene, effectively disrupting its intrinsic interlayer polar interactions that drive self-aggregation. By enveloping asphaltene aggregates as a "molecular coating", NaDES not only introduces steric hindrance but also modifies the effective solvation layer via its lipophilic groups (e.g., alkyl chains in TDA). This dual mechanism enhances colloidal stability, allowing the system to tolerate higher concentrations of *n*-heptane without precipitation. This enhancement substantially exceeds the 1.1-fold improvement reported for imidazolium ionic liquids by Boukherissa et al. (2009). These results unequivocally demonstrate that NaDES additives profoundly alter the thermodynamics of the flocculation process, directly evidencing DES's superior solvation capability for asphaltenes.

As shown in Fig. 5(d, e), the contact angle measurements demonstrate that NaDES exhibits significantly superior wettability compared to water and dodecylbenzenesulfonic acid (DBSA) on asphaltene surfaces. Initial contact angles reveal hydrophobic characteristics for both water (136.7°) and DBSA solution (117.5°) ($\theta > 90°$), while NaDES shows a markedly lower initial contact angle of 55°, indicating its exceptional wetting capability. Dynamic observations further demonstrate that the NaDES contact angle rapidly decreases to 10.4° within 300 ms, approaching complete spreading ($\theta \rightarrow 0°$), confirming its instantaneous penetration ability. According to the Young–Dupré equation (Emamian et al., 2019), the solid–liquid interfacial energy (ΔG) can be expressed as follows (Wang et al., 2022):

$$\Delta G = \gamma[1 + \cos(\theta)] \quad (1)$$

where γ represents the surface tension of the solvent; θ is the contact angle between the solvent and the asphaltene.

NaDES possesses an intrinsically lower surface tension ($\gamma_{NaDES} = 31.2$ mN/m; $\gamma_{DBSA} = 39.9$ mN/m) and a significantly lower viscosity ($\eta_{NaDES} = 23.7$ mPa·s; $\eta_{DBSA} \approx 900$ mPa·s). Calculations reveal that NaDES significantly reduces the interfacial energy ($\Delta G = 12.3–12.6$ mN/m), nearly half that of the commercial dispersant DBSA. This superior performance stems from a synergistic combination of its inherent surfactant properties and strong hydrogen-bonding interactions with asphaltenes, which enable rapid, near-instantaneous restructuring of the interface (Lemaoui et al., 2022). Acting as an integrated "solvent–surfactant" system, NaDES not only promotes effective solvent diffusion but also stabilizes the interface through dual physicochemical mechanisms.

Through a self-prepared two-dimensional porous media model, the static dissolution process of asphaltene particles in NaDES was investigated. As shown in Fig. 5(f), the initial contours of the asphaltene particles were clearly visible in the model. Over time, the particle boundaries became blurred, accompanied by the appearance of darker regions around the particles, indicating asphaltene dissolution. Concurrently, the surface area of the particles increased. Analysis of the particle diffusion area ratio (defined as the actual particle area divided by the initial particle area) revealed that the ratio reached its maximum value of

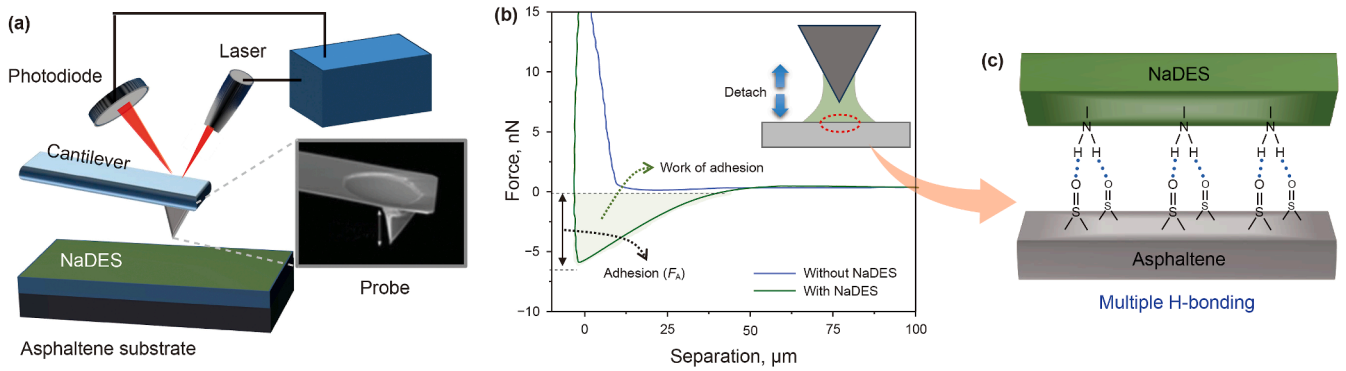

Fig. 6. (**a**) Schematic of the microprobe technique. (**b**) Force–distance curves acquired on a NaDES-covered asphaltene substrate. The bidirectional arrow indicates the adhesion force (F_A), while the highlighted area corresponds to the work of adhesion. (**c**) Schematic of the adhesion mechanism.

approximately 4.5 after 3 h, demonstrating the relatively high diffusion coefficient of asphaltene in NaDES solvent.

To better investigate the adhesive interaction between NaDES and asphaltene, we used probe atomic force microscopy (AFM) to measure adhesion on thin asphaltene layers. This technique enables precise measurement of normal-direction adhesion forces through probe retraction from planar substrates (Butt et al., 2005) (Fig. 6(a)). The resulting force–distance curves reveal the adhesion force (F_A), defined as the maximum negative force during retraction (Fig. 6(b)), which must be overcome for the detachment. In control experiments measuring the adhesion on bare asphaltene layers (without NaDES), we observed negligible adhesion forces (Fig. 6(b)). However, when testing the NaDES-coated asphaltene system, the hydrophobic NaDES (contact angle of <10°) demonstrated strong probe affinity. During detachment, NaDES bridge formed between the probe and asphaltene layer (Fig. 6(b) inset), resulting in a significantly enhanced adhesion force of −6.7 nN. The corresponding work of adhesion, calculated from the area under the retraction curve (bright green region in Fig. 6(b)), further confirmed this strengthened interaction. This pronounced adhesion enhancement primarily stems from multiple H-bonding between NaDES and asphaltene (Fig. 6(c)) (Makvandi et al., 2022).

The microstructural evolution of asphaltenes before and after dissolution was investigated using SEM and TEM. The raw asphaltene sample appeared as coarse particles covered with fine particulate matter (Fig. 7(c–f)). In contrast, after treatment with a NaDES, the asphaltenes underwent significant etching and were transformed into micro-/nano-sheet structures with smoother surfaces and more distinct layered stacking (Fig. 7(a, b, d, e)). TEM-EDS elemental mapping revealed that these nanosheets were predominantly composed of carbon, followed by oxygen, nitrogen, and sulfur, indicating a carbon-dominated framework with heteroatoms mainly distributed on the surface. XRD provided quantitative insight into the corresponding structural changes (Fig. 7(g)). The patterns displayed three characteristic peaks: the γ-band (~20°) associated with aliphatic chains, the (002) band (~25°) reflecting aromatic-sheet stacking, and the (10) band (~43°)

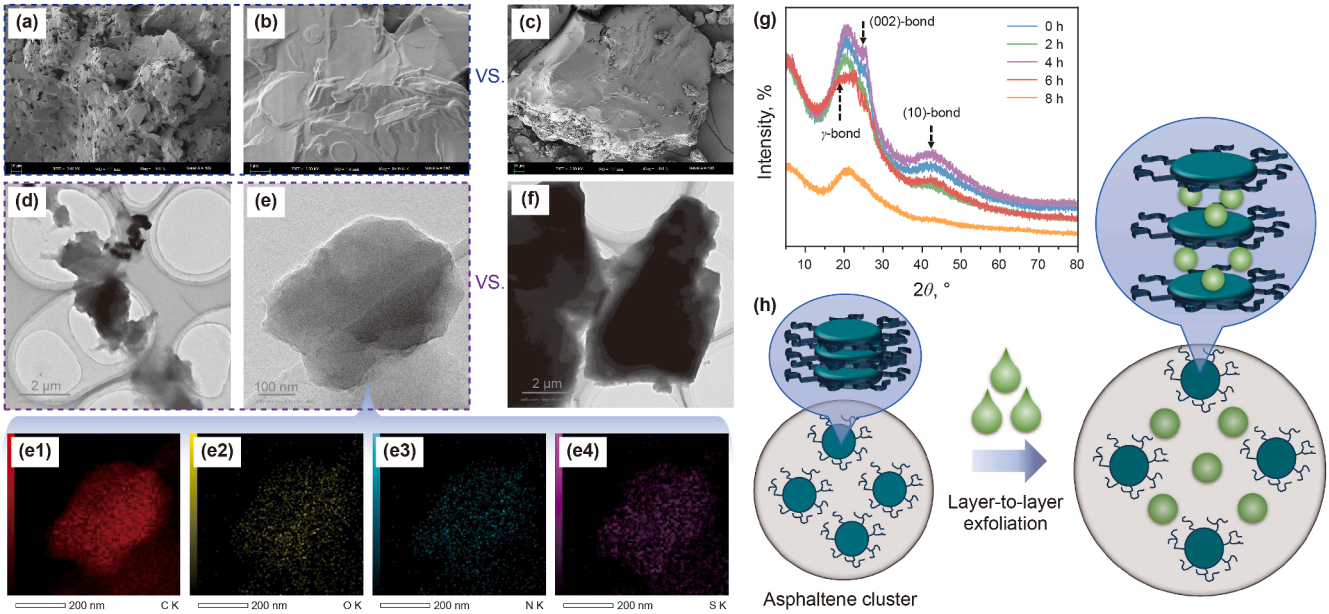

Fig. 7. (**a**, **b**) SEM images of the NaDES-treated asphaltene sample. (**c**) SEM images of asphaltene sample. (**d**, **e**) TEM images of the NaDES-treated asphaltene sample and its corresponding elemental maps for carbon (C), oxygen (O), nitrogen (N), and sulfur (S) (e1–e4). (**f**) TEM images of asphaltene sample. (**g**) XRD of bituminous samples treated with NaDES. (**h**) Schematic diagram showing the stepwise dissociation of asphaltene macromolecular clusters into smaller molecules.

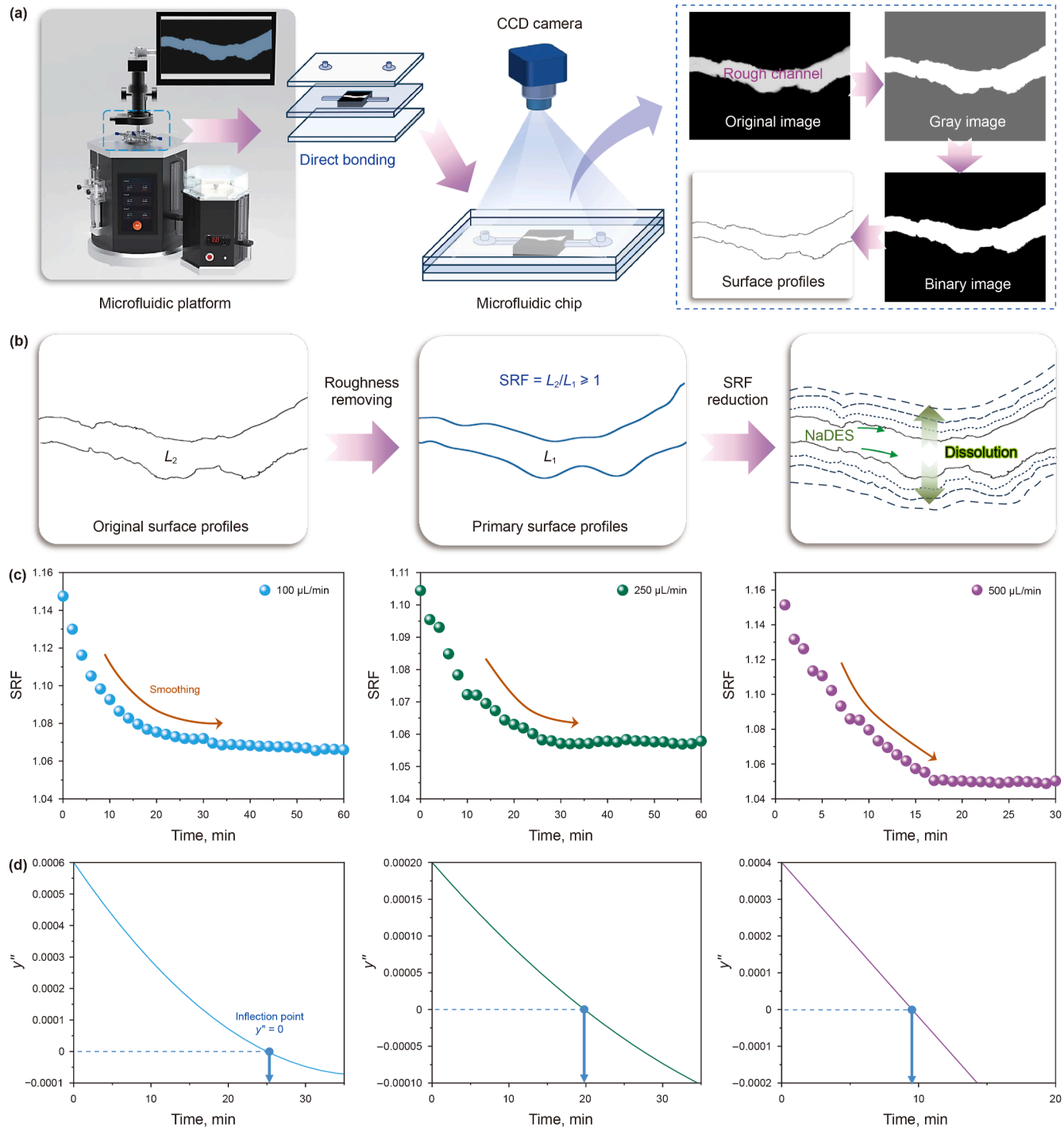

Fig. 8. (**a**) Experimental setup for dissolution observation at the channel scale. (**b**) The CCD images show asphaltenes (dark) and NaDES (white), and after grayscale/binary processing, fluid–solid interfaces appear as boundary curves. The SRF (small-scale features of less than 250 μm removed via MATLAB) is used to quantify roughness. (**c**) The evolutions of the rough surfaces (i.e., SRF) with increasing injection volume. (**d**) The second derivatives of the fitting curves of the surface roughness factor (y''), where the inflection point is t_c.

related to in-plane ordering of aromatic rings. With prolonged NaDES treatment, these peaks shifted and their intensities changed. Quantitative analysis (Table S8) showed an increase in both aliphatic interchain spacing (d_γ) and interlayer spacing between aromatic sheets (d_m), while the stacking height (L_c), layer diameter (L_a), and number of layers per stack (M) decreased. These results demonstrate that NaDES molecules intercalate between the aromatic layers, competitively weakening the native π-π stacking through competing π-interactions and steric effects, thereby expanding the interlayer distance and loosening the overall stacked architecture (AlHumaidan et al., 2015).

FT-IR analysis (Fig. S4(a)) provides complementary molecular-level evidence for the structural expansion induced by NaDES. The disappearance of amine bands and the emergence of O–H

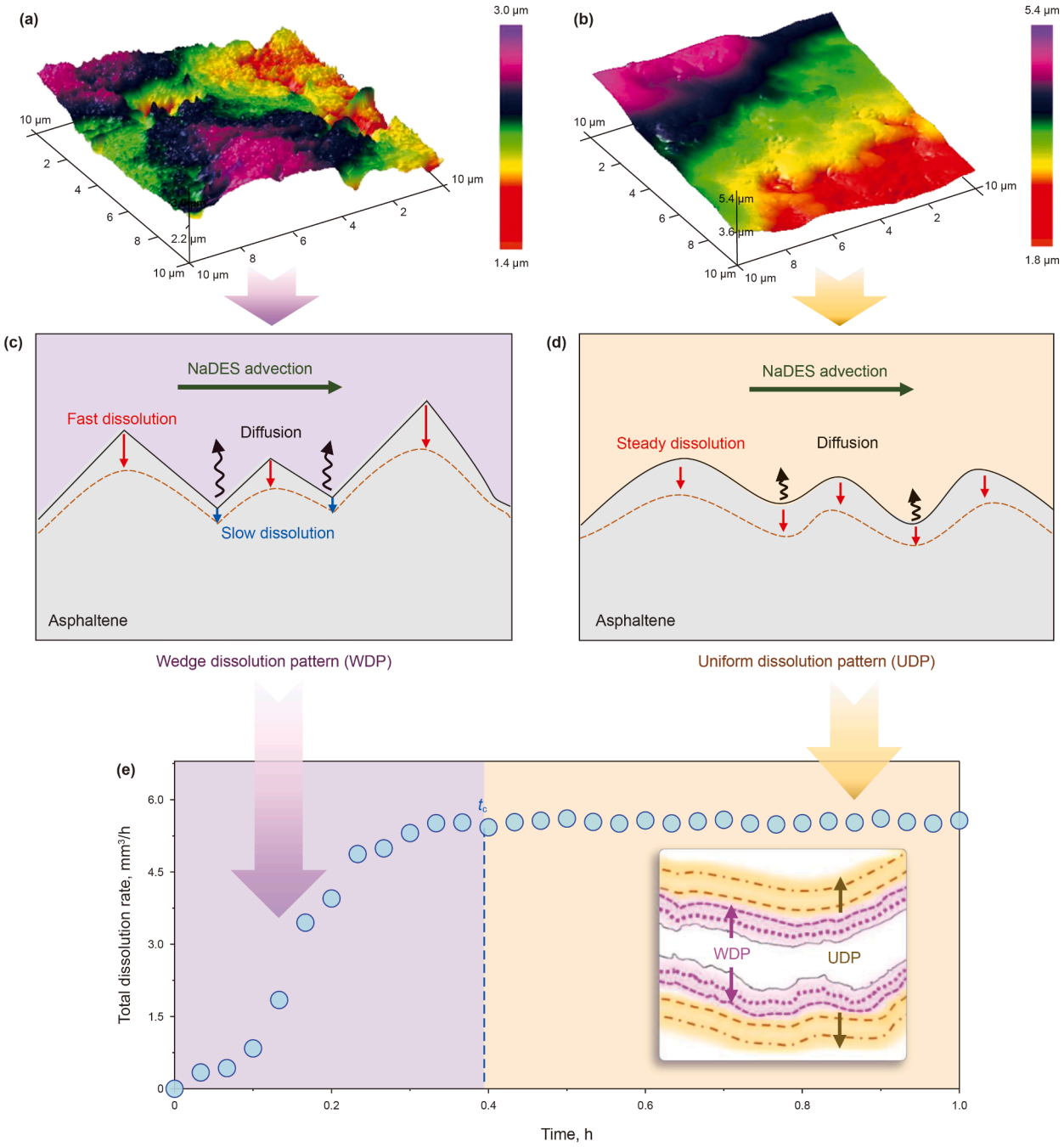

Fig. 9. Three-dimensional AFM images of the asphaltene surface before (**a**) and after (**b**) NaDES treatment. (**c**, **d**) Schematic representation of the effect of different surface roughness on dissolution patterns. (**e**) Total dissolution rate (R_t) as a function of time at a flow rate of 100 μL/min.

stretching vibrations directly corroborate the hydrogen-bonding interactions (–NH_2···O=S) predicted by DFT calculations. Quantitatively, as shown in Fig. S4(b), the increase in aliphatic/aromatic ratio (from 5.02 to 10.83) and the decrease in hydrogen aromaticity (from 0.79 to 0.65) further reflect the preferential retention of aliphatic chains and enhanced condensation of aromatic systems (Lemaoui et al., 2022). Meanwhile, the TG/DTG analysis results of this study lend further support to the above conclusions (Fig. S5), which indicates that the NaDES-treated asphaltenes exhibit a more pronounced mass loss rate in the low-temperature region (100−300 °C), which corresponds to more distinct thermal relaxation during the glass transition. This change is possibly related to the weakening of π-π interactions between the aromatic layers in supramolecular structure, providing key thermal analysis evidence that NADES effectively disrupts the originally tight, intrinsic stacking of asphaltenes. These spectral changes, together with the exfoliated sheet-like morphology (TEM, SEM) and increased interlayer spacing (XRD), consistently demonstrate that NaDES selectively disrupts π-π stacking between aromatic cores via competitive hydrogen-bond insertion, leading to the disassembly of aggregates into smaller clusters and a more open microstructure (Fig. 7(h)).

In summary, the rapid dissolution of asphaltenes by a NaDES can be attributed to the following mechanisms: (1) Interfacial

adhesion and wetting: Hydrogen bonding and van der Waals interactions between NaDES and asphaltenes significantly reduce interfacial energy and enhance adhesion (adhesion force: −6.7 nN), facilitating rapid spreading of the solvent on the asphaltene surface (contact angle close to 0°). (2) Penetration and diffusion: The alkyl chains of NaDES penetrate the layered aggregates of asphaltenes, disrupting intermolecular π-π stacking and promoting solvent diffusion, as reflected by a diffusion area ratio of 4.5. (3) Layer-to-layer exfoliation: The etching effect exfoliates the asphaltene surface, leading to disintegration into micro-nano sheets. (4) Dispersion stability: After dissolution, solvent–graphene interactions balance the inter-sheet attractive forces, resulting in stable dispersion, evidenced by a threefold increase in the precipitation point of asphaltenes in poor solvents.

3.4. Pore-scale dissolution behaviour in rough channels

To investigate the evolution of pore-scale channel surfaces during asphaltene dissolution, a microfluidic device was constructed and the raw images were captured using a CCD camera (Fig. 8(a)). After grayscale conversion and binarization, the fluid–solid interfaces were represented by boundary curves between the two phases (Fig. 8(b)). To evaluate interface roughness and elucidate its influence on the reaction rate, the surface roughness factor (SRF) is introduced and defined as the ratio of the total original profile length (L_2) to the total primary profile length (L_1):

$$\mathrm{SRF} = \frac{L_2}{L_1} \tag{2}$$

Using MATLAB polynomial filtering and wavelet decomposition, the original rough surface profile was decomposed into 8 levels. Based on the trend of variance change, the sixth level was selected as the optimal truncation level, successfully separating the primary undulations (large-scale geometric features) from the small-scale random roughness. As shown in Fig. 8(c), the SRF variation is used to characterize the micropore dissolution behavior under different *Pe* (*Pe* is the ratio of convection to diffusion, which can be calculated from Eq. (S7) in Supplementary Information) values (Table S6). The SRF profile shows an initial gradual decrease followed by stabilization, with the transition timing exhibiting clear flow-rate dependence. At high *Pe*, SRF decreases rapidly in the initial stage of dissolution, whereas SRF decreases with a lower rate for a small *Pe*. The critical transition time (t_c) is defined as the inflection point of the fitted SRF curve, which corresponds to where its second derivative equals zero (Fig. 8(d)). From Fig. S6, the critical transition time decreases with increasing average flow velocity, which indicates that higher flow velocities accelerate the transition from the rapid smoothing stage of the initial surface roughness to the stable dissolution stage.

The smoothing effect of NaDES on asphaltene surfaces was verified by AFM (Fig. 9(a, b)), whereas the NaDES-treated surface showed a markedly smoother topography while retaining its underlying undulations (Fig. 9(b)). Quantitative roughness parameters confirm this smoothing effect (Table S9). The root-mean-square roughness (R_q), arithmetic mean deviation (R_a), and maximum roughness (R_{max}) decreased from 188, 154, and 1277 nm to 151, 115, and 953 nm, respectively, with a reduction of 20%−25%. These results demonstrate that NaDES penetrates surface pores and depressions, reducing microscale irregularities through asphaltene dissolution and molecular redistribution.

To quantitatively investigate the influence of surface morphology on dissolution behavior, we analyze the relationship between roughness smoothing and the overall dissolution rate (R_t). Here, R_t is defined as the dissolved volume per unit time, calculated as follows (Zhou et al., 2019):

$$R_t = \frac{\Delta V_t}{\Delta t} = \frac{\int_0^{L_0} [\Delta S_u(x) + \Delta S_d(x)] W \mathrm{d}x}{\Delta t} \tag{3}$$

where L_0 is the channel length; W is the channel thickness. Since the overall dissolution rate is the average value within a specific time interval (t), the total dissolved area $\Delta S_u(x) + \Delta S_d(x)$ is calculated from t to $t + \Delta t$. The pore-scale dissolution dynamics evolve through two distinct temporal stages (Fig. 9(c–e)): an initial stage ($t < t_0$), where the overall dissolution rate (R_t) increases linearly alongside significant surface smoothing, followed by a later stage ($t > t_0$), where R_t stabilizes to a constant value. In the initial stage (low *Pe*, high Da_{II}; Da_{II} is a dimensionless parameter quantifying the relative effects of dissolution and diffusion, as given by Eq. (S8) in Supplementary Information), rapid surface reaction and flow-velocity gradients establish transverse concentration gradients in concave regions, rendering dissolution diffusion-limited. In convex regions adjacent to main flow channels, advection dominates and rapidly removes dissolved asphaltenes. The flow-field distribution governs the dissolution pattern, producing a wedge-shaped dissolution front (WDP) (Fig. 9(c)) with fast dissolution at peaks and slow dissolution in troughs, consistent with a mass-transport-limited regime (Roded et al., 2020). In the later stage (high $Pe \gg 1$, low Da_{II}), the preferential dissolution of peaks drives the system toward equilibrium diffusion conditions. Advection surpasses the reaction rate, enabling rapid replenishment of reactive fluid and homogenization of the concentration field, which yields a uniform dissolution pattern (UDP) (Fig. 9(d)) and the observed surface smoothing (Zhou et al., 2022).

4. Conclusions

In this work, a newly developed green and low-toxicity NaDES (thymol/TDA) demonstrated superior dissolution capacity for asphaltene deposits (approximately 75 mg/mL at 25 °C), significantly outperforming conventional toluene/*n*-heptane mixed solvents (8–10 mg/mL). The thymol/TDA combination was identified as optimal by screening 676 DESs with the COSMO-RS method. Density-functional theory (DFT) calculations revealed that the dissolution mechanism is governed by hydrogen bonding (notably between the $-NH_2$ group in NaDES and S=O in asphaltene) and dispersive interactions. This performance is attributed to a synergistic mechanism: (i) interfacial adhesion and near-complete wetting (contact angle of ~0°) driven by reduced interfacial energy, (ii) penetration of alkyl chains disrupting π-π stacking and promoting diffusion, (iii) layer-to-layer exfoliation breaking asphaltenes into micro-nano sheets, and (iv) enhanced dispersion stability, tripling the precipitation point of asphaltenes in poor solvents. Microfluidic visualization further quantified the dissolution dynamics, showing a surface smoothing effect and a flow-rate-dependent transition from a wedge-shaped to a uniform dissolution pattern.

CRediT authorship contribution statement

Ya-Han Liu: Writing – original draft. **Xin-Yi Ma:** Data curation. **Ding-Kai Hu:** Formal analysis. **Qiang Wang:** Investigation. **Peng Wei:** Writing – review & editing. **Hui Sun:** Writing – review & editing, Supervision.

Declaration of competing interest

The authors declare that they have no known competing financial interests or personal relationships that could have appeared to influence the work reported in this paper.

Acknowledgements

This work was sponsored by the National Natural Science Foundation of China (22208274), the Key Research and Development Projects of Xinjiang Uygur Autonomous Region (2025B01008-1 and 2024B01018-2), and the Tianshan Talents Science and Technology Innovation Team (2024TSYCTD0004).

Appendix A. Supplementary data

Supplementary data to this article can be found online at https://doi.org/10.1016/j.petsci.2026.04.015.

References

Abbott, A.P., Capper, G., Davies, D.L., et al., 2003. Novel solvent properties of choline chloride/urea mixtures. Chem. Commun. (1), 70–71. https://doi.org/10.1039/B210714G.

Ainurofiq, A., Mauludin, R., Mudhakir, D., et al., 2018. A novel desloratadine-benzoic acid co-amorphous solid: Preparation, characterization, and stability evaluation. Pharmaceutics 10 (3), 85. https://doi.org/10.3390/pharmaceutics10030085.

AlHumaidan, F.S., Hauser, A., Rana, M.S., et al., 2015. Changes in asphaltene structure during thermal cracking of residual oils: XRD study. Fuel 150, 558–564. https://doi.org/10.1016/j.fuel.2015.02.076.

Alioui, O., Benguerba, Y., Alnashef, I.M., 2020. Investigation of the CO_2-solubility in deep eutectic solvents using COSMO-RS and molecular dynamics methods. J. Mol. Liq. 307, 113005. https://doi.org/10.1016/j.molliq.2020.113005.

Altamash, T., Nasser, M.S., Elhamarnah, Y., et al., 2018. Gas solubility and rheological behavior study of betaine and alanine based natural deep eutectic solvents (NADES). J. Mol. Liq. 256, 286–295. https://doi.org/10.1016/j.molliq.2018.02.049.

Barrera, D.M., Ortiz, D.P., Yarranton, H.W., et al., 2013. Molecular weight and density distributions of asphaltenes from crude oils. Energy Fuels 27 (5), 2474–2487. https://doi.org/10.1021/ef400142v.

Behloul, H., Ferkous, H., Bougdah, N., et al., 2022. New insights on the adsorption of CI-Reactive Red 141 dye using activated carbon prepared from the $ZnCl_2$-treated waste cotton fibers: Statistical physics, DFT, COSMO-RS, and AIM studies. J. Mol. Liq. 364, 119956. https://doi.org/10.1016/j.molliq.2022.119956.

Benguerba, Y., Alnashef, I.M., Erto, A., et al., 2019. A quantitative prediction of the viscosity of amine based DESs using Sσ-profile molecular descriptors. J. Mol. Struct. 1184, 357–363. https://doi.org/10.1016/j.molstruc.2019.02.052.

Benítez, J.J., San-Miguel, M.A., Domínguez-Meister, S., et al., 2011. Structure and chemical state of octadecylamine self-assembled monolayers on mica. J. Phys. Chem. 115 (40), 19716–19723. https://doi.org/10.1021/jp203871g.

Boukherissa, M., Mutelet, F., Modarressi, A., et al., 2009. Ionic liquids as dispersants of petroleum asphaltenes. Energy Fuels 23 (5), 2557–2564. https://doi.org/10.1021/ef800629k.

Butt, H.J., Cappella, B., Kappl, M., 2005. Force measurements with the atomic force microscope: Technique, interpretation and applications. Surf. Sci. Rep. 59 (1), 1–152. https://doi.org/10.1016/j.surfrep.2005.08.003.

Chutia, S., Narzari, R., Bordoloi, N., et al., 2018. Pyrolysis of dried black liquor solids and characterization of the bio-char and bio-oil. Mater. Today Proc. 5 (11), 23193–23202. https://doi.org/10.1016/j.matpr.2018.11.050.

Conn, C.A., Ma, K., Hirasaki, G.J., et al., 2014. Visualizing oil displacement with foam in a microfluidic device with permeability contrast. Lab. Chip. Roy. Soc. Chem. 14 (20), 3968–3977. https://doi.org/10.1039/C4LC00620H.

Długosz, O., Banach, M., 2024. Sunlight photobiocatalytic performance of LDH-Me_2O nanocomposites synthesised in deep eutectic solvent (DES). Solid State Sci. 149, 107456. https://doi.org/10.1016/j.solidstatesciences.2024.107456.

Emamian, S., Lu, T., Kruse, H., et al., 2019. Exploring nature and predicting strength of hydrogen bonds: A correlation analysis between atoms-in-molecules descriptors, binding energies, and energy components of symmetry-adapted perturbation theory. J. Comput. Chem. 40 (32), 2868–2881. https://doi.org/10.1002/jcc.26068.

Fan, D., Xie, X., Li, C., et al., 2021. Extraction of noncondensed lignin from poplar sawdusts with *p*-toluenesulfonic acid and ethanol. J. Agric. Food Chem. 69 (37), 10838–10847. https://doi.org/10.1021/acs.jafc.1c03774.

Gao, N., Wang, Y., Luo, H., et al., 2024. pH-switchable hydrophobic deep eutectic solvents for sustainable recycling extraction of high oily waste. Chem. Eng. J. 495, 153339. https://doi.org/10.1016/j.cej.2024.153339.

Hebbar, A., Debraj, D., Acharya, S., et al., 2023. Deep eutectic solvents interaction with asphaltenes: A combined experimental and molecular dynamics study. J. Mol. Liq. 387, 122627. https://doi.org/10.1016/j.molliq.2023.122627.

Jahangiri, S., Shahrabadi, A., Heydari, A., et al., 2017. Choline chloride/monoethylene glycol deep eutectic solvent as a new asphaltene precipitation inhibitor. Pet. Sci. Technol. 35 (19), 1896–1902. https://doi.org/10.1080/10916466.2017.1369116.

Jiang, G., He, K., Chen, M., et al., 2025. Improvement of mechanical and bioactive properties of chitosan films plasticized with novel thymol-based deep eutectic solvents. Food Hydrocoll. 158, 110480. https://doi.org/10.1016/j.foodhyd.2024.110480.

Kim, M., Sell, A., Sinton, D., 2013. Aquifer-on-a-chip: Understanding pore-scale salt precipitation dynamics during CO_2 sequestration. Lab Chip 13 (13), 2508–2518. https://doi.org/10.1039/c3lc00031a.

Kumar, N., Mhapsekar, U., Banerjee, T., 2024. Dispersion stability mechanism of asphaltene in deep eutectic solvents through multiresolution simulation approaches. Ind. Eng. Chem. Res. 63 (50), 22005–22017. https://doi.org/10.1021/acs.iecr.4c02351.

Lan, S.S., Li, Y.F., Xue, S., et al., 2021. Application of deep eutectic solvents modified oxidized hydrogen-substituted graphyne in adsorption and electrochemistry. J. Mol. Liq. 335, 116532. https://doi.org/10.1016/j.molliq.2021.116532.

Lemaoui, T., Boublia, A., Darwish, A.S., et al., 2022. Predicting the surface tension of deep eutectic solvents using artificial neural networks. ACS Omega 7 (36), 32194–32207. https://doi.org/10.1021/acsomega.2c03458.

Lemaoui, T., Darwish, A.S., Attoui, A., et al., 2020a. Predicting the density and viscosity of hydrophobic eutectic solvents: Towards the development of sustainable solvents. Green Chem. 22 (23), 8511–8530. https://doi.org/10.1039/d0gc03077e.

Lemaoui, T., Darwish, A.S., Hammoudi, N.E.H., et al., 2020b. Prediction of electrical conductivity of deep eutectic solvents using COSMO-RS sigma profiles as molecular descriptors: A quantitative structure–property relationship study. Ind. Eng. Chem. 59 (29), 13343–13354. https://doi.org/10.1021/acs.iecr.0c02542.

Li, J.G., Guo, X., Shen, H.P., et al., 2021. The solubility of asphaltene in organic solvents and its relation to the molecular structure. J. Mol. Liq. 327, 114826. https://doi.org/10.1016/j.molliq.2020.114826.

Majka, T.M., Bednarz, S., Pielichowski, K., 2025. Green deep eutectic solvents (DESs) as a sustainable solution for thermal stabilization and flame retardancy of key bioplastic-polylactide. Thermochim. Acta 753, 180155. https://doi.org/10.1016/j.tca.2025.180155.

Makvandi, P., Maleki, A., Shabani, M., et al., 2022. Bioinspired microneedle patches: Biomimetic designs, fabrication, and biomedical applications. Matter 5 (2), 390–429. https://doi.org/10.1016/j.matt.2021.11.021.

Mullins, O.C., Sabbah, H., Eyssautier, J., et al., 2012. Advances in asphaltene science and the Yen–Mullins model. Energy Fuels 26 (7), 3986–4003. https://doi.org/10.1021/ef300185p.

Neni, A., Boublia, A., Bouras, M., et al., 2024. Evaluating asphaltene dispersion with choline chloride or menthol based deep eutectic solvents: A COSMO-RS analysis. J. Mol. Liq. 407, 125272. https://doi.org/10.1016/j.molliq.2024.125272.

Parsai, G., Parikh, P.A., Parikh, J.K., 2024. Novel DES- ultrasonication assisted process for nanocellulose synthesis using box behnken design. Ind. Crops Prod. 217, 118856. https://doi.org/10.1016/j.indcrop.2024.118856.

Roded, R., Aharonov, E., Holtzman, R., et al., 2020. Reactive flow and homogenization in anisotropic media. Water Resour. 56 (12). https://doi.org/10.1029/2020WR027518.

Sellaoui, L., Dotto, G.L., Peres, E.C., et al., 2017. New insights into the adsorption of crystal violet dye on functionalized multi-walled carbon nanotubes: Experiments, statistical physics and COSMO–RS models application. J. Mol. Liq. 248, 890–897. https://doi.org/10.1016/j.molliq.2017.10.124.

Shafique, S., Belousov, A.S., Rashid, R., et al., 2025. Deep eutectic solvents (DES): Structure, properties, and cutting-edge applications in green catalysis. J. Mol. Liq. 419, 126769. https://doi.org/10.1016/j.molliq.2024.126769.

Slavov, D., Tomaszewska, E., Grobelny, J., et al., 2024. FTIR spectroscopy revealed nonplanar conformers, chain order, and packaging density in diOctadecylamine- and octadecylamine-passivated gold nanoparticles. J. Mol. Struct. 1314, 138827. https://doi.org/10.1016/j.molstruc.2024.138827.

Sukor, N.F., Selvam, V.P., Jusoh, R., et al., 2021. Intensified DES mediated ultrasound extraction of tannic acid from onion peel. J. Food Eng. 296, 110437. https://doi.org/10.1016/j.jfoodeng.2020.110437.

Trenzado, J.L., Benito, C., Escobedo-Monge, M.A., et al., 2023. Cineole – decanoic acid hydrophobic natural deep eutectic solvent for toluene absorption. J. Mol. Liq. 384, 122036. https://doi.org/10.1016/j.molliq.2023.122036.

Wang, W., Zhu, B., Xu, Y., et al., 2022. Mechanism study of ternary deep eutectic solvents with protonic acid for lignin fractionation. Bioresour. Technol. 363, 127887. https://doi.org/10.1016/j.biortech.2022.127887.

You, J., Lee, K.J., 2021. A pore–scale investigation of surface roughness on the evolution of natural fractures during acid dissolution using DBS method. J. Pet. Sci. Eng. 204, 108728. https://doi.org/10.1016/j.petrol.2021.108728.

Zainal-Abidin, M.H., Hayyan, M., Ngoh, G.C., et al., 2019. Emerging frontiers of deep eutectic solvents in drug discovery and drug delivery systems. J. Control. Release 316, 168–195. https://doi.org/10.1016/j.jconrel.2019.09.019.

Zhou, C.X., Hu, R., Li, H.W., et al., 2022. Pore-scale visualization and quantification of dissolution in microfluidic rough channels. Water Resour. 58 (11). https://doi.org/10.1029/2022WR032255.

Zhou, J.Q., Wang, L., Chen, Y.F., et al., 2019. Mass transfer between recirculation and main flow zones: Is physically based parameterization possible? Water Resour. 55 (1), 345–362. https://doi.org/10.1029/2018wr023124.